Unveiling the cellular microstructure–property relations in martensitic stainless steel via laser powder bed fusion

Lingzhi Wu, Cong Zhang, Dil Faraz Khan, Ruijie Zhang, Yongwei Wang, Xue Jiang, Haiqing Yin, Xuanhui Qu, Geng Liu, and Jie Su

Articles you may be interested in

De-cheng Kong, Chao-fang Dong, Xiao-qing Ni, Liang Zhang, Rui-xue Li, Xing He, Cheng Man, and Xiao-gang Li, Microstructure and mechanical properties of nickel-based superalloy fabricated by laser powder-bed fusion using recycled powders, *Int. J. Miner. Metall. Mater.*, 28(2021), No. 2, pp. 266-278. https://doi.org/10.1007/s12613-020-2147-4

Jin-hua Zhou, Yong-feng Shen, and Nan Jia, Strengthening mechanisms of reduced activation ferritic/martensitic steels: A review, *Int. J. Miner. Metall. Mater.*, 28(2021), No. 3, pp. 335-348. https://doi.org/10.1007/s12613-020-2121-1

Peng-fei Wang, Ming Liang, Xiao-yan Xu, Jian-qing Feng, Cheng-shan Li, Ping-xiang Zhang, and Jin-shan Li, Effect of groove rolling on the microstructure and properties of Cu–Nb microcomposite wires, *Int. J. Miner. Metall. Mater.*, 28(2021), No. 2, pp. 279-284. https://doi.org/10.1007/s12613-020-2073-5

Mehmet Akif Erden and Fatih Aydın, Wear and mechanical properties of carburized AISI 8620 steel produced by powder metallurgy, *Int. J. Miner. Metall. Mater.*, 28(2021), No. 3, pp. 430-439. https://doi.org/10.1007/s12613-020-2046-8

Hui-ping Duan, Xiao Liu, Xian-zhe Ran, Jia Li, and Dong Liu, Mechanical properties and microstructure of 3D-printed high Co-Ni secondary hardening steel fabricated by laser melting deposition, *Int. J. Miner. Metall. Mater.*, 24(2017), No. 9, pp. 1027-1033. https://doi.org/10.1007/s12613-017-1492-4

Xing-hai Yang, Xiao-hua Chen, Shi-wei Pan, Zi-dong Wang, Kai-xuan Chen, Da-yong Li, and Jun-wei Qin, Microstructure and mechanical properties of ultralow carbon high-strength steel weld metals with or without Cu–Nb addition, *Int. J. Miner. Metall. Mater.*, 28(2021), No. 1, pp. 120-130. https://doi.org/10.1007/s12613-020-2159-0

IJMMM WeChat

QQ author group

Unveiling the cellular microstructure–property relations in martensitic stainless steel via laser powder bed fusion

Lingzhi Wu[1], *Cong Zhang*[1),✉], *Dil Faraz Khan*[2], *Ruijie Zhang*[1,4),✉], *Yongwei Wang*[1], *Xue Jiang*[1,3,4],
Haiqing Yin[1,3,4),✉], *Xuanhui Qu*[1,3,4,5], *Geng Liu*[6], *and Jie Su*[6]

1) Collaborative Innovation Center of Steel Technology, University of Science and Technology Beijing, Beijing 100083, China

2) Department of Physics, University of Science and Technology Bannu, Bannu 28100, Pakistan

3) Beijing Advanced Innovation Center for Materials Genome Engineering, University of Science and Technology Beijing, Beijing 100083, China

4) Beijing Key Laboratory of Materials Genome Engineering, University of Science and Technology Beijing, Beijing 100083, China

5) Institute for Advanced Materials and Technology, University of Science and Technology Beijing, Beijing 100083, China

6) Institute for Special Steel Research, Central Iron and Steel Research Institute, Beijing 100081, China

(Received: 25 March 2024; revised: 28 May 2024; accepted: 29 May 2024)

Abstract: Laser powder bed fusion (LPBF) is a widely recognized additive manufacturing technology that can fabricate complex components rapidly through layer-by-layer formation. However, there is a paucity of research on the effect of laser scanning speed on the cellular microstructure and mechanical properties of martensitic stainless steel. This study systematically investigated the influence of laser scanning speed on the cellular microstructure and mechanical properties of a developed Fe11Cr8Ni5Co3Mo martensitic stainless steel produced by LPBF. The results show that increasing the laser scanning speed from 400 to 1000 mm/s does not lead to a noticeable change in the phase fraction, but it reduces the average size of the cellular microstructure from 0.60 to 0.35 μm. The scanning speeds of 400 and 1000 mm/s both had adverse effects on performances of sample, resulting in inadequate fusion and keyhole defects respectively. The optimal scanning speed for fabricating samples was determined to be 800 mm/s, which obtained the highest room temperature tensile strength and elongation, with the ultimate tensile strength measured at (1088.3 ± 2.0) MPa and the elongation of (16.76 ± 0.10)%. Furthermore, the mechanism of the evolution of surface morphology, defects, and energy input were clarified, and the relationship between cellular microstructure size and mechanical properties was also established.

Keywords: laser powder bed fusion; martensitic stainless steel; cellular microstructure; mechanical properties; strengthening mechanism

1. Introduction

Metal additive manufacturing, with its rapid capabilities and high design flexibility [1–2], is suitable for the direct shaping of metals with complex geometrical structures [3–4] and is widely used in aerospace, nuclear industry, biomedical, and other fields [3,5–6]. Martensitic stainless steel, renowned for its high strength and excellent weldability, is well-suited for additive manufacturing [7], and also demonstrates superior mechanical strength and corrosion resistance [8]. The Fe–Cr–Ni–Co–Mo alloy representing a novel, cost-effective, ultra-high strength, and high toughness martensitic stainless steel has attracted widespread attention from researchers [9–11].

In additive manufacturing, the laser powder bed fusion (LPBF) is widely recognized for its capability to fabricate intricate parts [12–13]. Although the geometric control of LPBF-produced components is generally well-managed, the optimization of their microstructure and mechanical proper-

ties remains a challenging problem [14–15]. In fact, due to the complex thermal history induced by LPBF process, the microstructure and mechanical behavior depend on the heat input [16–18]. The heat input is affected by various forming process parameters, including scanning speed [12–19], laser power [20–21], hatch space [15], scanning mode [22], etc. In other words, processing parameters have a significant influence on the microstructure and mechanical properties of additively manufactured alloys.

Over the past few years, extensive researches have focused on the interplay between process parameters, microstructure, and properties of LPBF stainless steels. Liu *et al.* [23] analyzed the impact of scanning speed on the microstructure and mechanical properties of 316L austenitic stainless steel and revealed that high scanning speed (1000 mm/s) results in a high proportion of low-angle grain boundaries and refined grains, enhancing the maximum tensile strength. Conversely, low scanning speeds (800 mm/s) minimize residual pores and melt pool boundaries, achieving a maxim-

Springer

um elongation up to 55% [23]. By optimizing the scanning speed, Nigon *et al.* [24] successfully produced 2205 austenitic–ferritic stainless steel samples with a relative density of 98.6% using the LPBF process. Furthermore, Jiang *et al.* [25] studied the effect of LPBF laser scanning speed on the forming performance, microstructural evolution, wear, and corrosion resistance of ferritic stainless steel, discovering that increased scanning speed induce the anisotropic microstructures enriched with low-angle grain boundaries and α-Fe. The microhardness was measured to be HV 812, and the specific wear rate was found to be 1.99×10^{-6} mm³/(N·m). Similarly, it was demonstrated that the microstructure of 17-4 PH martensitic stainless steel produced by LPBF process can be tailored to improve its mechanical properties by adjusting laser power, scanning speed, and hatch distance [26–27].

From the brief overview of the literature, it is evident that most of the research has focused on the effects of process parameters on the microstructure and properties of LPBF-316L austenitic stainless steel and LPBF martensitic precipitation-hardened stainless steel. While additional studies have examined 17-4PH martensitic stainless steel [28–29] and 18Ni300 martensitic stainless steel [30–31], there is a paucity of research on the effect of scanning speed on the cellular microstructure and mechanical properties of martensitic stainless steel produced via LPBF. Consequently, this study is designed to explore the phase and cellular microstructural characterisics of Fe11Cr8Ni5Co3Mo martensitic stainless steel produced by LPBF under various laser scanning speeds. The Fe11Cr8Ni5Co3Mo martensitic stainless steel, developed by our team, is a cost-effective material with superior properties

[9–11]. Furthermore, tensile performance tests were conducted on the as-fabricated specimens at room temperature. The objective of this research was to establish the relationship between laser scanning speed, cellular microstructure, phase evolution, and mechanical properties of Fe11Cr8Ni5Co3Mo steel produced via LPBF processing.

2. Experimental

2.1. Raw material

In this study, the low-carbon high-alloy martensitic stainless steel powder with a nominal composition of Fe11Cr8Ni5Co3Mo was used as raw material. The powder was produced through vacuum plasma rotating electrode atomization by Zhonghang Maite Powder Manufacturer (China). The chemical composition of the powder was analyzed using the Shimadzu EMIA-820A carbon-sulfur analyzer, the full spectrum direct-reading inductively coupled plasma emission spectrometer, and TCH600 oxygen-nitrogen-hydrogen analyzer. The results of powder composition are presented in Table 1. The morphology of the powder is shown in Fig. 1(a), while the particle size distribution is illustrated in Fig. 1(b), most of the particles fall within the diameters of 16.3–58.0 μm.

Table 1.   Chemical composition of the martensitic stainless steel wt%

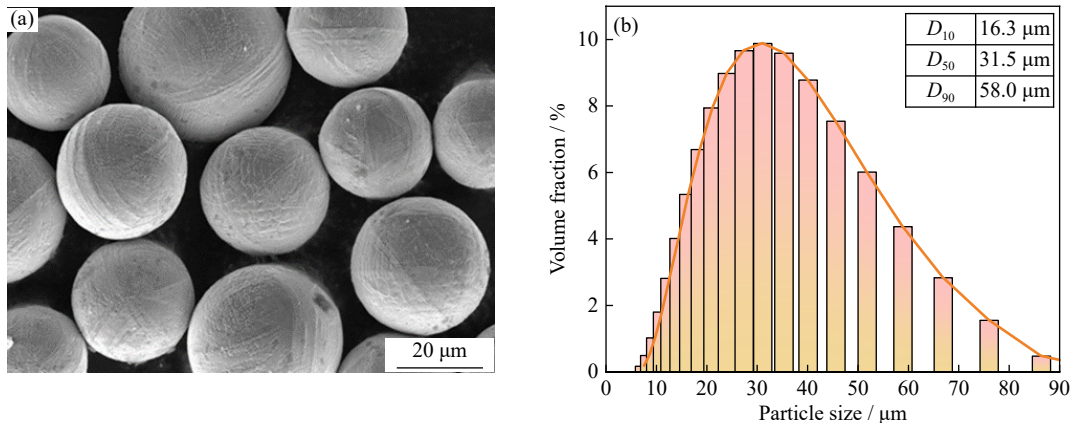| Fe	Cr	Ni	Mo	Co	Mn	V	Al	Si	C
Bal.	11.3	8.0	3.0	4.37	0.26	0.14	0.20	0.22	0.018

Fig. 1.   (a) Powder morphology and (b) particle size distribution of raw material (D_{10}, D_{50}, and D_{90} represent the particle sizes when the cumulative particle size distribution reaches 10vol%, 50vol%, and 90vol% respectively).

2.2. Processing parameters

In this study, the martensitic stainless steel were produced via LPBF in an SLM125HL system (Germany), equipped with Yb-Fiber laser. The printing atmosphere was Ar, the oxygen content was controlled below 0.12wt%, and a rotation angle of 67° between the neighboring layers was chosen to be the scanning strategy. The scanning speed was varied from 400 to 1000 mm/s. The substrate was made of 316L stainless steel, and the preheating temperature of the substrate was 200°C. The volumetric energy density *E* with the

unit of J/mm³ was calculated as follows [15,32–33]:

$$E = \frac{P}{v \cdot h \cdot d} \tag{1}$$

where *P*, *v*, *h*, and *d* represent the laser power (W), scan speed (mm/s), hatch distance (μm), and layer thickness (μm), respectively. The detailed processing parameters and energy density are listed in Table 2.

2.3. Characterizations

Basic observations of the morphology of the FeCrNiCo-Mo martensitic stainless steel melt pool were conducted us-

2478

Int. J. Miner. Metall. Mater., Vol. 31, No. 11, Nov. 2024

ing an optical microscope (DM4000, Leika). Scanning electron microscopy (SEM, GeminiSEM500, Zeiss) and transmission electron microscopy (TEM, FEI Talos F200X) were used to observe the powder and the microstructure of the LPBF-FeCrNiCoMo martensitic stainless steel, including the fracture morphology of the tensile specimens. The phase constitution and crystal structure of the sample was performed using an Ultima IV X-ray diffractometer (XRD, SmartLab). The XRD operated at a copper target X-ray tube with a voltage of 40 kV, a current of 40 mA, and a scanning

step size of 0.2°/min.

The tensile performance test was based on the ASTM E8/E8M standard (ISO 6892-1:2009) and followed the GB/T 228-2010 standard. The gauge length of tensile specimens was 15 mm. The tests were carried out at room temperature and on an electronic universal testing machine with a stretching rate of 0.5 mm/min. Engineering stress–strain curves were obtained and further converted into true stress–strain curves. Fig. 2 illustrates the schematic diagram of the printed block and printed tensile specimen.

Table 2.   Processing parameter configuration for different samples

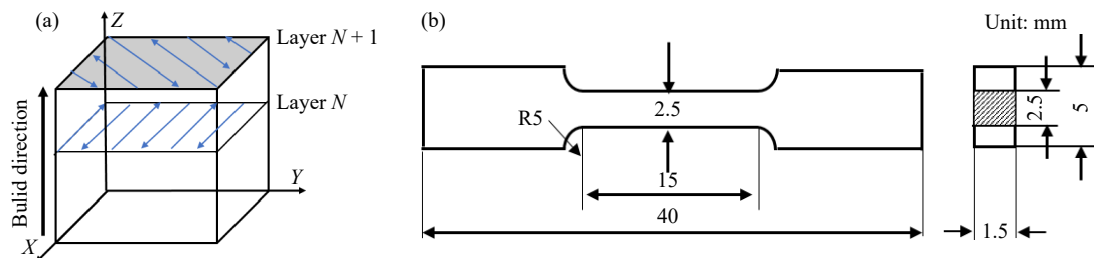| Sample	Laser power / W	Scanning speed / (mm·s^{-1})	Hatch distance / μm	Layer thickness / μm	Energy density / (J·mm^{-3})
1	100	400	100	20	125.0
2	100	600	100	20	83.3
3	100	800	100	20	62.5
4	100	1000	100	20	50.0

Fig. 2.   Schematic illustration of sample: (a) printed block with its scanning strategy; (b) dimensions of the tensile specimen.

3. Results

3.1. Phase analysis

The XRD analysis results of FeCrNiCoMo martensitic stainless steel prints corresponding to different scanning speed is shown in Fig. 3.

The phase structure of the as-printed martensitic stainless steel primarily consists of martensite with a lesser amount of austenite, as observed from the diffraction peaks. The volume fraction of austenite can be estimated by comparing the integrated intensities of the (*hkl*) peaks in the XRD diffractogram using the following formulas [34]:

$$V_\gamma + V_{\alpha'} = 1 \tag{2}$$

$$V_\gamma = 1.4I_\gamma / (I_{\alpha'} + 1.4I_\gamma) \tag{3}$$

where V_γ and $V_{\alpha'}$ are the volume fractions of austenite and

martensite respectively, and I_γ and $I_{\alpha'}$ are the peak intensities of γ(111) and α′(110) respectively [35–36]. The calculated austenite content is approximately 2.5%. From Fig. 3, varying the scanning speed in the XRD spectra indicates that there is no significant change in the basic phases. However, there is a slight shift in the phase peaks under the same crystal plane, which is attributed to the solid solution effect and lattice distortion that occur during the printing process.

3.2. Microstructure characterization

3.2.1. Metallography

The macroscopic morphology of the scanning track and the melt pool of the samples under the laser power of 100 W and scaning speeds of 400, 600, 800, and 1000 mm/s are shown in Fig. 4.

Fig. 4 depicts a macroscopic melt pool image of the printed sample under optical microscopy. Through multiple microscopic observations and over 8 times of dimension measurements, as shown in Fig. 4(a), at a scanning speed of 400 mm/s, the melt pool is quite large with a depth of about (120 ± 10) μm, and it has a considerable number of defects such as lack of fusion porosity. In Fig. 4(b), at a scanning speed of 600 mm/s, the melt pool becomes wider and slightly shallower with a depth of about (80 ± 10) μm. Fig. 4(c) shows that the melt pool is more regular with a depth of about (50 ± 5) μm, and it has the least number of defects and a good width-to-depth ratio. In Fig. 4(d), the scanning speed is 1000 mm/s, the melt pool is relatively shallow with a depth of $(40 \pm$
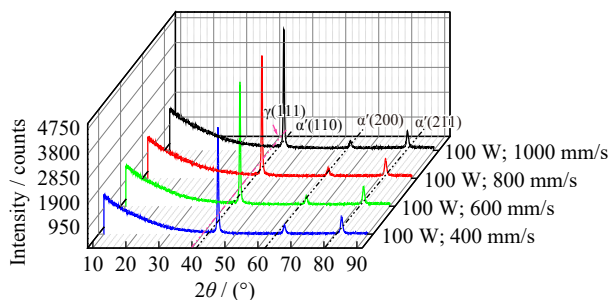

Fig. 3.   XRD patterns for FeCrNiCoMo martensitic stainless steel printed with different scanning speeds.
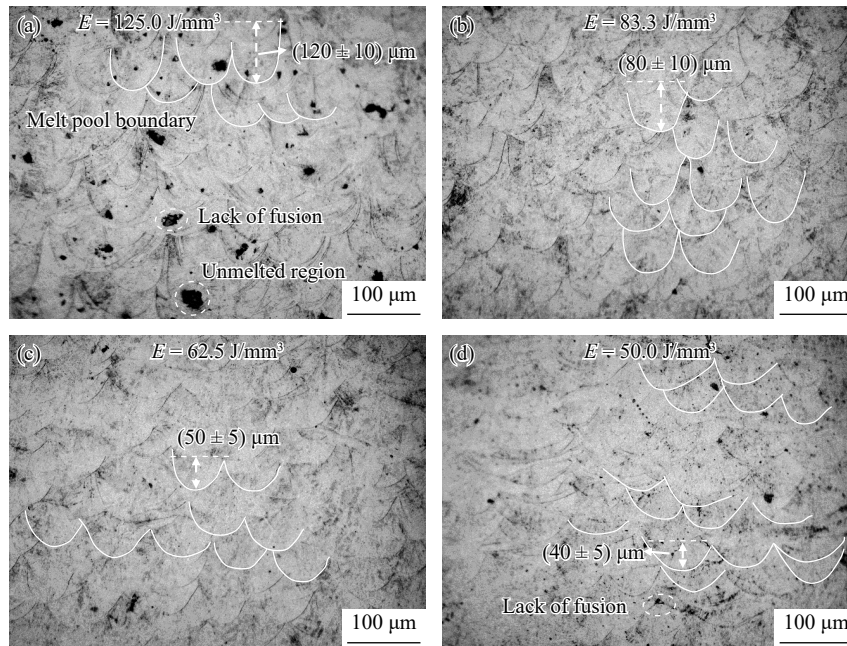
Fig. 4. Metallographic micrographs of LPBF-FeCrNiCoMo martensitic stainless steel printed with different scanning speeds: (a) 400 mm/s; (b) 600 mm/s; (c) 800 mm/s; (d) 1000 mm/s.

5) µm, and there is some unmelted region in the specimen.

This further verifies that as the scanning speed increases, the depth of the melt pool decreases and the width-to-depth ratio gradually increases [21,37]. The phenomenen is due to that when scanning speed increases, the average time that laser energy acts on the powder material shortens, the input of laser energy decreases, and the size of the melt pool decreases accordingly [37]. Consequently, the space range for grain growth also reduces [38]. As the scanning speed decreases, the depth of the melt pool increases correspondingly, which could lead to the evaporation of elements within the melt pool and the formation of porosity. Additionally, materials within the melt pool may experience splashing and ejection, contributing to the formation of keyholes and a significant reduction in density. This also results in balling effect, decreasing the compactness and roughening the surface of the specimen [39–40].

However, when the scanning speed is too high, it may cause incomplete melting of the powder and induce sphericalization, thus leading to poor interlayer bonding. Therefore, an optimal scanning speed is necessary to control the defects of LPBF materials.

3.2.2. Microstructure

Fig. 5 shows the microstructure inside the melt pool parallel to the building direction in images (a), (c), (e), and (g) on the left, and perpendicular to the building direction in images (b), (d), (f), and (h) on the right. The columnar grains grow fully in the direction parallel to building direction, and the columnar grains grow mainly towards the opposite temperature gradient direction, growing from the bottom of the melt pool to the center of the melt pool. The microstructure depends on the temperature gradient (G) and solidification rate (R) [41]. The G/R determines the supercooling of the composition before the melt pool solidifies [42]. Different areas inside the melt pool have different G/R values, leading to cer-

tain differences in the internal microstructure [43]. The temperature gradient at the edge of the melt pool is higher than that at the center. Subject to rapid re-heating and re-cooling cycles, a large number of quenched equiaxed grains are formed [11,44].

The cellular microstructure diameter of the plane perpendicular to the building direction decreases gradually with the increase of scanning speed, and the total number of cellular microstructures in the same area also increases. According to the microstructure characterization from multiple positions of specimen, the quantity of cells and average cellular microstructure size are shown in Table 3. It is obvious that the average cellular microstructure size decreased with the decrease of energy density. This is because a smaller melt pool can transfer heat more quickly with the surrounding area, and is conducive to the rapid nucleation of cellular microstructure, which in turn makes the average cellular microstructure size smaller [11].

3.2.3. Cellular microstructure

Fig. 6 shows the TEM micrographs of LPBF-FeCrNiCoMo martensitic stainless steel printed at scanning speed of 1000 mm/s. The dominant composition of the matrix organization is martensite, with minimal presence of residual austenite detected [45]. The mean width of the martensite laths is approximately 170 nm, and there are a large number of dislocation entanglements between the martensite layers [46]. The selected area diffraction pattern (SADP) in Fig. 6(b) shows it to be martensite. It was proposed that extreme cooling can result in a full martensitic transformation for LPBF [22], and the rapid transformation of martensite can generate many dislocations [47–48]. Studies indicate that the presence of residual austenite is closely related to the grain size of the parent austenite grain (PAG) [49]. In the vertical specimen, the size of the austenite lath is larger than the horizontal PAG size, resulting in less retention of austenite dur-
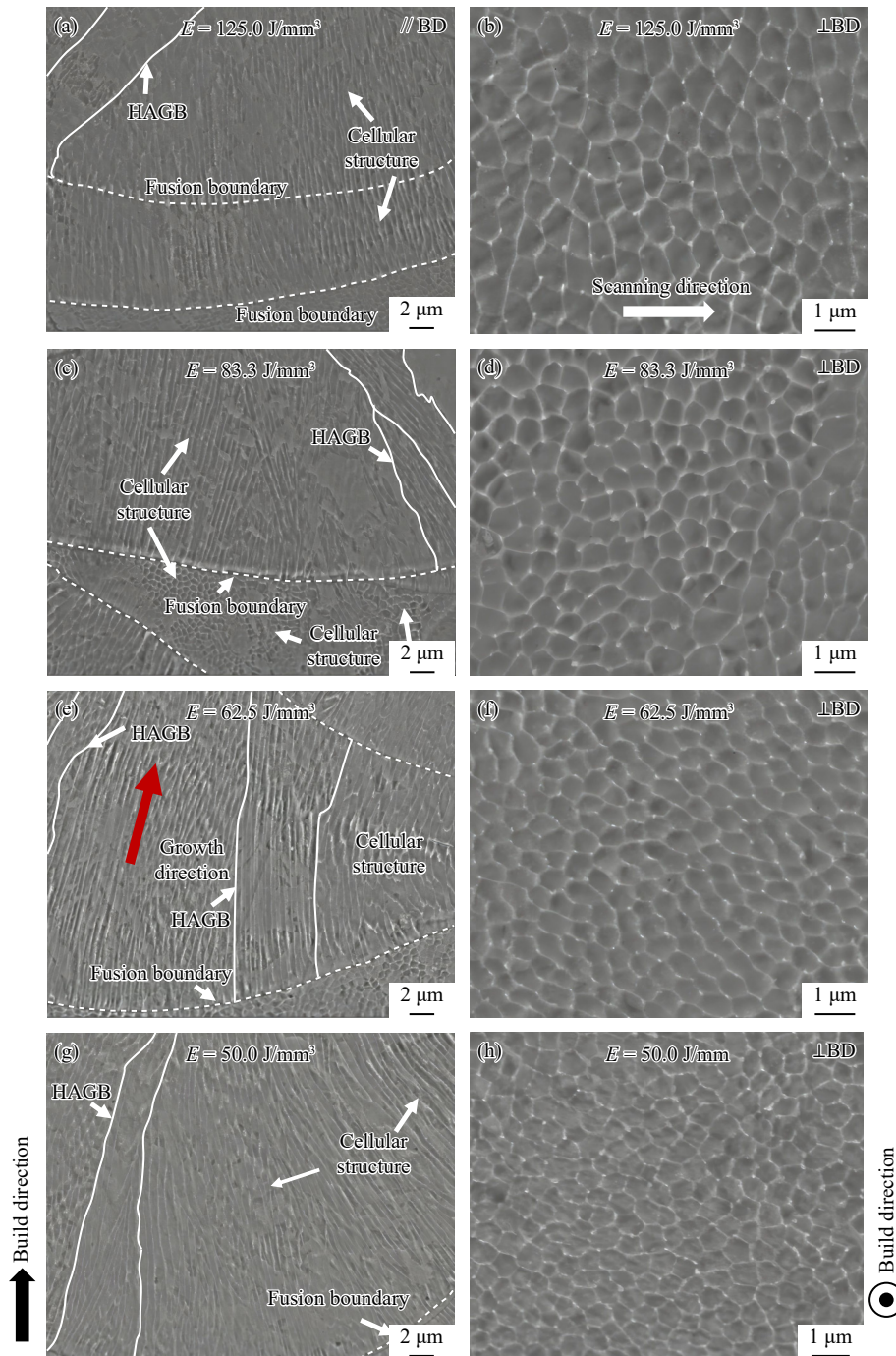
Fig. 5. Microstructure of LPBF-FeCrNiCoMo martensitic stainless steel under different scanning speeds: (a, b) 400 mm/s; (c, d) 600 mm/s; (e, f) 800 mm/s; (g, h) 1000 mm/s (the melt pool parallel to the build direction (BD) and perpendicular to BD are indicated on the left and right respectively; HAGB—high-angle grain boundaries).

Table 3. Relationship between scanning speed, energy density, and cellular microstructures

Energy density / (J·mm⁻³)	Scanning speed / (mm·s⁻¹)	Average numbers per view field	Cellular microstructure size / μm	Cross-sectional area of cellular microstructure / μm²
125.0	400	120–160	0.60 ± 0.20	1.10 ± 0.05
83.3	600	180–210	0.50 ± 0.20	0.78 ± 0.05
62.5	800	240–300	0.40 ± 0.10	0.50 ± 0.05
50.0	1000	300–350	0.35 ± 0.10	0.38 ± 0.10

ing the cooling process.

In order to identify the composition distribution within the cellular structure in detail, it was observed with a scanning

transmission electron microscopy (STEM) mode. Fig. 7(a) shows the bright-field (BF) image of the cellular structure of printed FeCrNiCoMo with scanning speed of 800 mm/s. The
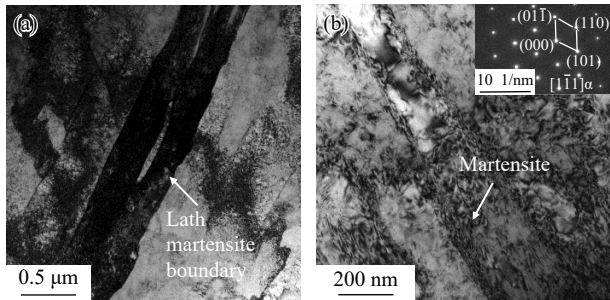
Fig. 6.   TEM micrographs of LPBF-FeCrNiCoMo martensitic stainless steel printed at scanning speed of 1000 mm/s: (a) low magnification; (b) high magnification (insert is the SADP of martensite).

morphology and grain size are consistent with the SEM observations in Fig. 5(f). Fig. 7(b) is a high-angle annular dark field (HAADF) mode, where many dislocation entanglements can be observed near the cellular structure [50]. The research on this martensitic stainless steel has revealed that as the cellular size decreases, the number of tangled dislocations gradually increases [11,51], which is manifested as an increase in the impediment to dislocations [52]. Fig. 7(c)–(h) shows the elemental segregation situation, with Fe, Cr, Co, Ni, and Mn showing detectable segregation. This segregation phenomenon can also be found in other LPBF materials with cellular structure [52].
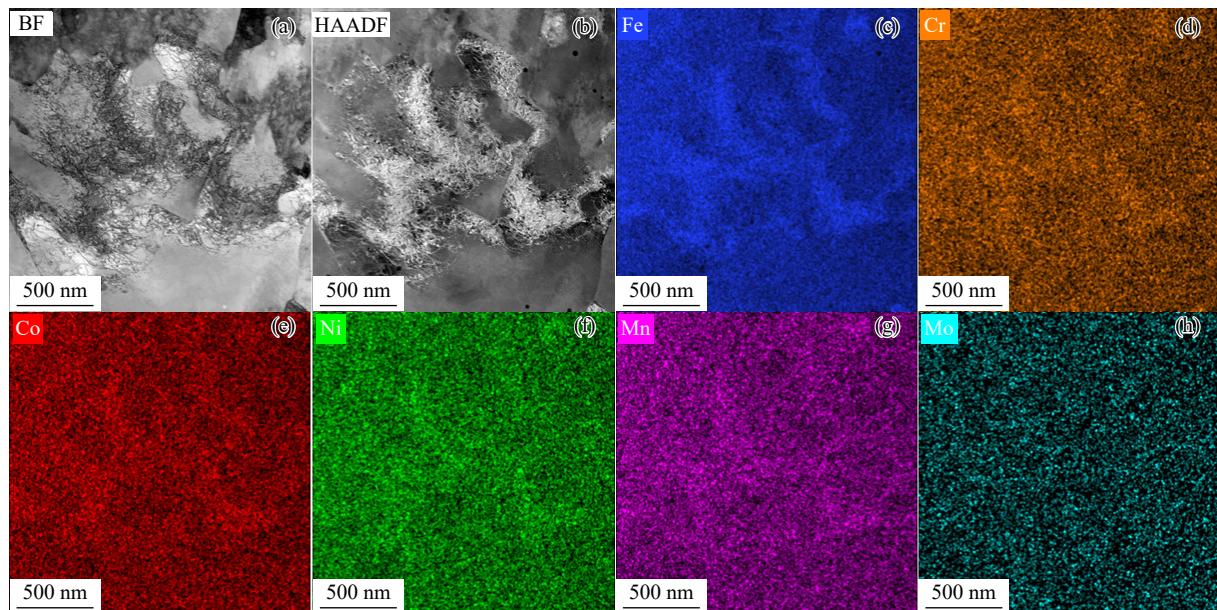

Fig. 7.   TEM images of the cellular structure in printed FeCrNiCoMo under scanning speed of 800 mm/s: (a) the cellular structure and its dislocations under BF mode; (b) the cellular structure and its dislocations under HAADF mode; (c–h) elemental segregation in the cellular structure.

3.3. Mechanical properties

Fig. 8 shows the tensile properties of the LPBF-FeCr-NiCoMo martensitic stainless steel under different laser scanning speeds, and the specific room-temperature tensile mechanical properties are presented in Table 4. Fig. 8(a) shows the representative individual tensile curves of each sample. Fig. 8(b) shows the average ultimate tensile strength (UTS) and elongation (EL) of samples, in which each experimental point is the average of five individual tests. As shown in Table 4 and Fig. 8(b), when the laser power is 100 W, the YS, UTS, and EL of the samples prepared by LPBF show an increase tendency with the increase of laser scanning speed from 400 to 800 mm/s and show a decrease tendency when scanning speed increase from 800 to 1000 mm/s. Therefore, sample 3 has the highest yield strength (YS) of (898.0 ± 2.0) MPa, highest UTS of (1088.3 ± 2.0) MPa, and optimal EL of (16.76 ± 0.10)%.

3.4. Fracture morphology

Fig. 9 shows the typical tensile fractures of the specimens

processed with a laser power of 100 W and scanning speeds of 400, 600, 800, and 1000 mm/s.

Fig. 9(a) shows that when the scanning speed is 400 mm/s, the fracture surface of the sample exhibits weak ductile fracture, with a large number of pores and inclusions inside dimples, and the elongation is only (13.91 ± 0.10)%. In Fig. 9(b)–(d), fine dimple features can be observed around the edges, with larger dimples present in the middle, which means that some shear planes fracture under applied stress conditions, forming fine dimple-like features. Fig. 9(b) shows that the toughness of the specimen at a scanning speed of 600 mm/s is slightly better than that at 400 mm/s, with an increase in the fine fibrous dimples, resulting in an elongation of (16.34 ± 0.10)% for the sample processed at 600 mm/s. As shown in Fig. 9(c), at a scanning speed of 800 mm/s, the specimen exhibits superior toughness, with an elongation of (16.76 ± 0.10)%. The interior features fine and uniform dimples with larger ones in the middle, and a significant necking is observed. Fig. 9(d) indicates that, compared to the samples scanned at 800 mm/s, there is a reduction in ductility–toughness at a scanning speed of 1000 mm/s, with an
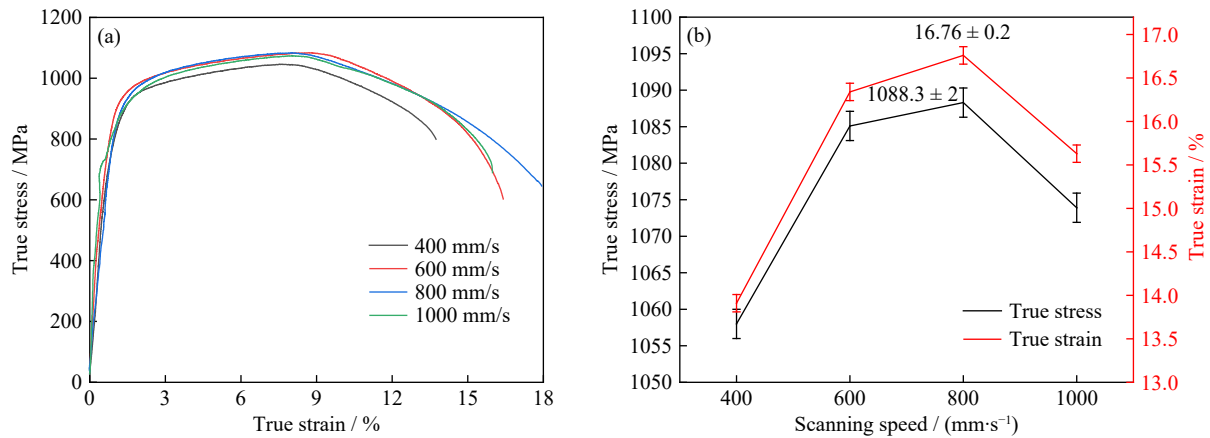
2482

Int. J. Miner. Metall. Mater., Vol. 31, No. 11, Nov. 2024

Fig. 8. True stress–strain curves of samples at different scanning speed: (a) representative curves and (b) the average value of UTS and EL.

Table 4. Mechanical properties of samples under different scanning speeds

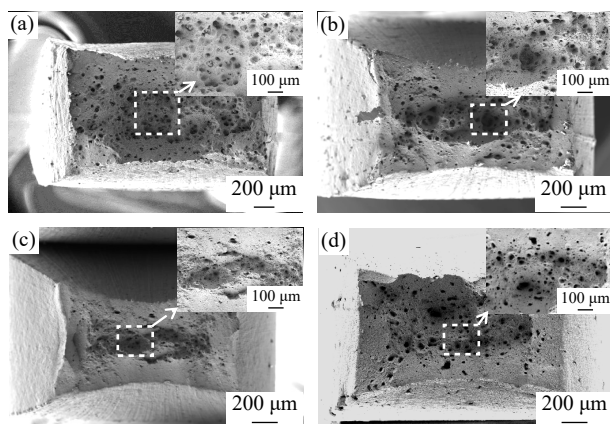| Scanning speed / (mm·s^{-1})	YS / MPa	UTS / MPa	EL / %
400	891.4 ± 1.0	1058.0 ± 2.0	13.91 ± 0.10
600	892.9 ± 2.0	1085.1 ± 2.0	16.34 ± 0.10
800	898.0 ± 2.0	1088.3 ± 2.0	16.76 ± 0.10
1000	776.9 ± 4.0	1073.9 ± 4.0	15.63 ± 0.10

Fig. 9. Tensile fracture morphology of LPBF-FeCrNiCoMo martensitic stainless steel with scanning speed of (a) 400 mm/s, (b) 600 mm/s, (c) 800 mm/s, and (d) 1000 mm/s.

elongation of (15.63 ± 0.10)%, due to a large number of unfused defects inside.

4. Discussion

4.1. Relationship between laser energy and defects

According to the scanning speed, the energy heat input of the laser can be categorized into three types [53], as shown in Fig. 10. When the laser power is fixed, the scanning speed is one of the key processing parameters in laser processing, which directly determines the heat input and temperature of the melt pool.

When the scanning speed is 400 mm/s, the longer the time spent on a unit area, which is referred to as "high energy." When the scanning speed is much higher (such as 1000 mm/s), the time spent on a unit area is shorter, which means

the powder receives "less energy." If the scanning speed is too high, it will result in the powder not being properly fused. Lack of fusion defects directly affect the interlayer bonding strength of the parts, making them more likely to break [54]. Moreover, these defects tend to have sharp edges that may cause stress concentration. The tips of the defects are often affected by thermal cycling in subsequent manufacturing processes, which can induce cracks [55]. When the scanning speed is 400 mm/s, the internal heat of the melt pool cannot be dissipated in time, which can lead to the evaporation of elements inside the melt pool and the formation of keyholes [56]. Therefore, gas pores and voids are generated. Pore defects have a negative impact on the tensile properties of materials [57–58]. When the scanning speed is appropriate, the energy density of the parts can be improved, and the defects of the parts can be significantly reduced. When the laser power is set at 100 W and the scanning speed is 800 mm/s, it constitutes the "optimum energy," achieving an optimal melting effect and maintaining excellent print quality.

4.2. Relationship between cellular structure and mechanical properties

As shown in Table 4 and Fig. 8, when the laser power is 100 W, with the increase of laser scanning speed from 400 to 800 mm/s, the YS, UTS, and EL of the samples prepared by LPBF show increase tendency. This can be related to the cellular structure, as previously mentioned, when the laser scanning speed increases, the obtained grain size decreases. The obtained small cellular structure (about 500 nm), as shown in Fig. 5, is significant for the ductility and strength of the material under working conditions [59]. However, when the scanning speed further increases to 1000 mm/s, both the strength and elongation of the sample decrease due to the reduction in heat input caused by the excessively high scanning speed [11,50], and there are more unmelted powders and irregular defects inside the sample [38,60].

Fig. 11 illustrates the fitted relationship between the cellular structure and mechanical properties at scanning speeds of 400–1000 mm/s. Fig. 11(a) and (b) shows the relationship between the cellular structure size and UTS and EL respectively. In Fig. 11(a), there is a parabolic relationship between equiaxed grain size and UTS, with a possible extreme value
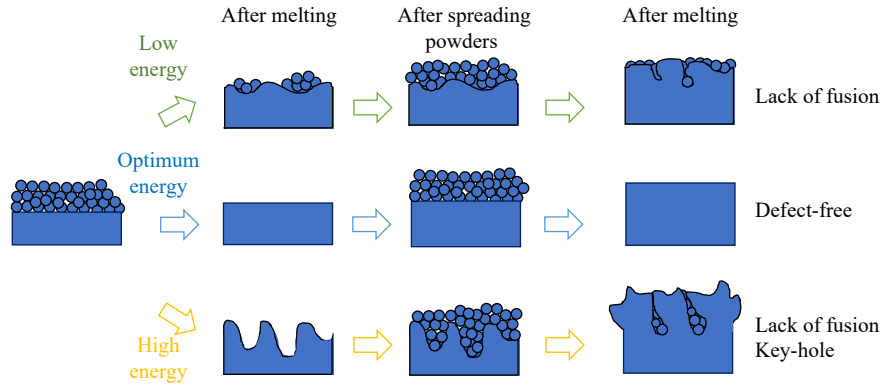
Fig. 10.   Schematic diagram of the mechanism between LPBF surface morphology, defects, and energy input.

of (1090 ± 5) MPa corresponding to an equiaxed grain size of 0.45 μm. When the cellular size is larger than 0.45 μm, the UTS shows a decreasing trend. The decrease of UTS may be due to the increased grain size, decreased dislocation density, and gradually increased material defects. In Fig. 11(b), there is also a parabolic relationship between the cellular size and EL, with the maximum EL possibly being (16.8 ± 0.2)%, corresponding to an equiaxed grain size of 0.45 μm. When

the cellular microstructure size of equiaxed grains is greater than 0.45 μm, the EL shows a decreasing trend because the increase in material defects. The fitted curve reflects the overall response of the cellular microstructure size and defects on mechanical properties, which indicates that the mechanical properties of the LPBF steel are more sensitive to cellular microstructure size, consisting with literature reports [61].
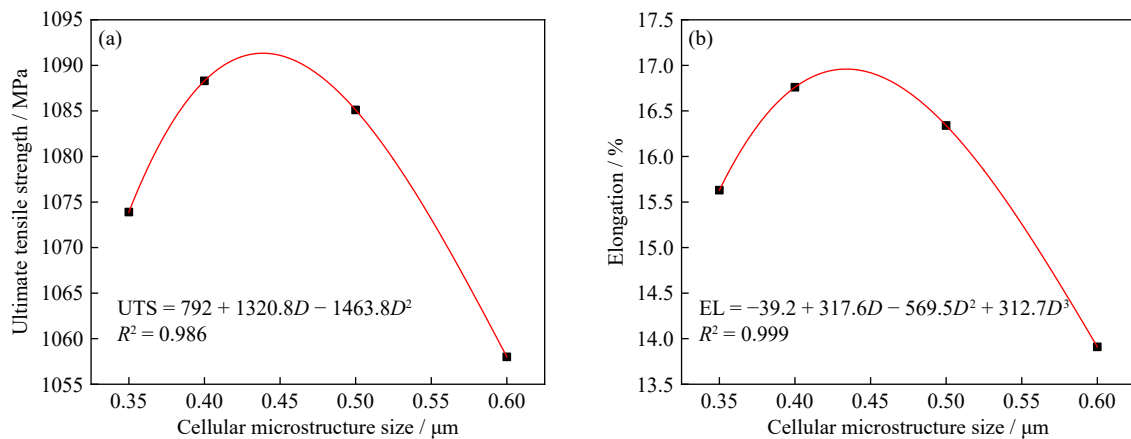

Fig. 11.   Relationship between the cellular structure of LPBF martensitic stainless steel and its mechanical properties: (a) the cellular structure size and UTS; (b) the cellular structure size (*D*) and EL.

4.3. Strengthening mechanism

The strengthening of martensitic aging steel relies on multiple mechanisms, and the contributions to the YS of martensitic stainless steel are generally considered to be four parts: (1) Martensite phase transformation strengthening σ_{Mart}; (2) Precipitation strengthening of intermetallic compounds σ_P; (3) Solid-solution strengthening σ_{SS}; (4) Residual austenite. Since the fraction of residual austenite is small (<1%), it can be ignored in this LPBF-FeCrNiCoMo martensitic stainless steel.

The YS of martensitic stainless steel can be represented by Eq. (4) [12,62]:

$$\sigma_Y = \sigma_0 + \sigma_{SS} + \sigma_{Mart} + \sigma_P \qquad (4)$$

where σ_0 is the lattice friction stress of martensitic stainless steel [63–65].

Martensitic phase transformation strengthening σ_{Mart} is generally controlled by grain boundary area (Hall-Petch ef-

fect) and dislocation density (Taylor equation) [66]. For steel with a carbon content less than 1wt%, the phase transformation strengthening formula is Eq. (5) [67].

$$\sigma_{Mart} = 300 \times D_{block}^{-1/2} + 0.25M\mu b\rho_{lath}^{1/2} \qquad (5)$$

where $M = 3$ is the Taylor orientation factor [67], $b = 0.286$ nm is the Burgers vector [66], $\mu = 71$ GPa is the shear modulus [68], D_{block} refers to the size of the martensite lath, which is generally 0.067 times the size of austenite [41–42] and block size $D_{block} = 1304$ nm [63], and $\rho_{lath} = 2.1 \times 10^{16}$ m^{-2} is the dislocation density under the printing state [11,68].

Solid-solution strengthening σ_{SS} is due to the increment of critical shear stress caused by the existence of substitutional solute atoms, which is estimated using the Fleischer equation [69–70]:

$$\sigma_{SS} = \sum \left(\beta_i^2 x_i\right)^{1/2} \qquad (6)$$

where x_i is the concentration of the solute element i in the alloy, and β_i is solid-solution strengthening coefficient of ele-

2484

Int. J. Miner. Metall. Mater., Vol. 31, No. 11, Nov. 2024

ment i, which quantifies the strengthening effect of the element, and its values are as shown in Table 5 [69–71]. In the existing steels, Ti and Mo have the greatest solid-solution strengthening effect, while Cr and V have the smallest effect.

Table 5. Solid-solution strengthening coefficient β_i

Ni	Ti	Mo	Co	Cr	V
334	2628	2143	334	174	134.6

Note: Assuming infinite solid solubility in Fe, and the effects of Al, Mn, and Si are generally considered negligible [66,72].

The strength increase caused by precipitation hardening σ_P can be attributed to the Orowan bypass or particle cutting phenomenon [73]. According to the analysis by Jin *et al.* [74], if the precipitates are only a few nanometers, the strengthening mechanism is mainly particle cutting, and Orowan strengthening can be considered. For nano-precipit-

ates at non-coherent interfaces, the Orowan mechanism can estimate the increase in strength, as shown in Eq. (7) [75–77]:

$$\sigma_P = \left(\frac{0.538 G b \sqrt{V_f}}{X}\right)\ln\left(\frac{X}{2b}\right) \qquad (7)$$

where G is the shear modulus 71 GPa, b is the Burgers vector, V_f is the volume fraction, and X is the diameter of the precipitate particle in nm, taken to be the equivalent spherical diameter. In the as-printed sample, no post-heat treatment was performed. From our previous work [11], the precipitates in the printed sample mainly consist of Al_2O_3 particles formed by some Al elements, with a size of about 100 nm.

By calculating Eqs. (5)–(7), the contributions of various strengthening mechanisms for yield strength were obtained. The final calculated results are listed in Table 6, and the contributions of the yield strength from various strengthening mechanisms are $\sigma_{Mart} > \sigma_{SS} > \sigma_P$. The calculated yield strength values are consistent with the experimental values.

Table 6. Comparison of calculated yield strength based on various strengthening mechanisms and experimental yield strength

Calculated strengthening contribution for σ_Y / MPa				Calculated σ_Y / MPa	Experimental YS / MPa
σ_0	σ_{Mart}	σ_{SS}	σ_P		
50	479.85	332.48	47.33	909.66	898.0 ± 2.0

5. Conclusions

The analysis of the microstructure and property research on martensitic stainless steel fabricated by LPBF under varying scanning speed has led to the following conclusions.

(1) The aspect ratio of the melt pool's dimensions increases with an increment in scanning speed. As the scanning speed rises from 400 to 1000 mm/s, the depth of the melt pool decreases successively from (120 ± 10) μm to (80 ± 10) μm, (50 ± 5) μm, and (40 ± 5) μm. Observing the macroscopic shape of the melt pool reveals a progressively flatter morphology.

(2) The microstructure of LPBF-FeCrNiCoMo primarily consists of nearly full martensite with a characteristic cellular structure typical of additive manufacturing. The cellular size in the plane perpendicular to the build direction diminishes as the scanning speed increases, with an average reduction from 0.60 to 0.35 μm. Segregation of elements such as Fe, Cr, Co, Ni, and minor Mn was observed at the cell walls. The scanning speed of 800 mm/s correlates with the least defects observed in this LPBF process.

(3) The mechanical properties are predominantly influenced by martensitic phase transformation strengthening. The tensile properties exhibit a trend of initial increase followed by a decrease; the peak UTS recorded is (1088.3 ± 2.0) MPa, with an EL of (16.76 ± 0.10)%, indicating a ductile fracture mode.

(4) A correlation has been identified between the cellular microstructure grain size and the mechanical properties of martensitic stainless steel in the as-printed condition. Within the scanning speed range of 400–1000 mm/s, the cellular microstructure size significantly influences the UTS and EL.

The UTS is defined by the equation UTS = $-1463.8D^2$ + $1320.8D$ + 792, while the EL is given by (EL = $312.7D^3$ − $569.5D^2$ + $317.6D$ − 39.2).

Conflict of Interest

Xuanhui Qu is an editorial board member for this journal and was not involved in the editorial review or the decision to publish this article. All authors state that there is no conflict of interest.

References

[1] Z.Y. Liu, D.D. Zhao, P. Wang, *et al*., Additive manufacturing of metals: Microstructure evolution and multistage control, *J. Mater. Sci. Technol.*, 100(2022), p. 224.

[2] H.L. Cheng, X.C. Luo, and X. Wu, Recent research progress on additive manufacturing of high-strength low-alloy steels: Focusing on the processing parameters, microstructures and properties, *Mater. Today Commun.*, 36(2023), art. No. 106616.

[3] J. Fu, H. Li, X. Song, and M.W. Fu, Multi-scale defects in powder-based additively manufactured metals and alloys, *J.*

Mater. Sci. Technol., 122(2022), p. 165.

[4] M. Simonelli, Z.Y. Zou, P. Barriobero-Vila, and Y.Y. Tse, The development of ultrafine grain structure in an additively manufactured titanium alloy via high-temperature microscopy, *Materialia*, 30(2023), art. No. 101856.

[5] T. DebRoy, H.L. Wei, J.S. Zuback, *et al.*, Additive manufacturing of metallic components–Process, structure and properties, *Prog. Mater. Sci.*, 92(2018), p. 112.

[6] J.L. Cann, A. De Luca, D.C. Dunand, *et al.*, Sustainability through alloy design: Challenges and opportunities, *Prog. Mater. Sci.*, 117(2021), art. No. 100722.

[7] C.L. Tan, K.S. Zhou, W.Y. Ma, P.P. Zhang, M. Liu, and T.C. Kuang, Microstructural evolution, nanoprecipitation behavior and mechanical properties of selective laser melted high-performance grade 300 maraging steel, *Mater. Des.*, 134(2017), p. 23.

[8] J.R. Lee, M.S. Lee, H. Chae, *et al.*, Effects of building direction and heat treatment on the local mechanical properties of direct metal laser sintered 15-5 PH stainless steel, *Mater. Charact.*, 167(2020), art. No. 110468.

[9] G. Liu, J. Su, A. Wang, *et al.*, A novel Fe–Cr–Ni–Co–Mo maraging stainless steel with enhanced strength and cryogenic toughness: Role of austenite with core-shell structures, *Mater. Sci. Eng. A*, 863(2023), art. No. 144537.

[10] D.H. Liu, J. Su, A. Wang, *et al.*, Tailoring the microstructure and mechanical properties of FeCrNiCoMo maraging stainless steel after laser melting deposition, *Mater. Sci. Eng. A*, 840(2022), art. No. 142931.

[11] L.Z. Wu, D.F. Khan, C. Zhang, *et al.*, Microstructure and mechanical characterization of additively manufactured Fe11Cr8Ni5Co3Mo martensitic stainless steel, *Mater. Charact.*, 203(2023), art. No. 113106.

[12] D.D. Dong, C. Chang, H. Wang, *et al.*, Selective laser melting (SLM) of CX stainless steel: Theoretical calculation, process optimization and strengthening mechanism, *J. Mater. Sci. Technol.*, 73(2021), p. 151.

[13] Y.X. Geng, H. Tang, J.H. Xu, *et al.*, Influence of process parameters and aging treatment on the microstructure and mechanical properties of AlSi8Mg3 alloy fabricated by selective laser melting, *Int. J. Miner. Metall. Mater.*, 29(2022), No. 9, p. 1770.

[14] G.Q. Dai, M.H. Xue, Y.H. Guo, *et al.*, Gradient microstructure and strength-ductility synergy improvement of 2319 aluminum alloys by hybrid additive manufacturing, *J. Alloys Compd.*, 968(2023), art. No. 171781.

[15] M.W. Vaughan, M. Elverud, J. Ye, *et al.*, Development of a process optimization framework for fabricating fully dense advanced high strength steels using laser directed energy deposition, *Addit. Manuf.*, 67(2023), art. No. 103489.

[16] X.D. Nong, X.L. Zhou, J.H. Li, Y.D. Wang, Y.F. Zhao, and M. Brochu, Selective laser melting and heat treatment of precipitation hardening stainless steel with a refined microstructure and excellent mechanical properties, *Scripta Mater.*, 178(2020), p. 7.

[17] W. Abd-Elaziem, S. Elkatatny, A.E. Abd-Elaziem, *et al.*, On the current research progress of metallic materials fabricated by laser powder bed fusion process: A review, *J. Mater. Res. Technol.*, 20(2022), p. 681.

[18] W. Abd-Elaziem, S. Elkatatny, T.A. Sebaey, M.A. Darwish, M.A. Abd El-Baky, and A. Hamada, Machine learning for advancing laser powder bed fusion of stainless steel, *J. Mater. Res. Technol.*, 30(2024), p. 4986.

[19] Q. Chen, L.Y. Xu, L. Zhao, K.D. Hao, and Y.D. Han, Effect of scanning speed on microstructure and mechanical properties of as-printed Ti–22Al–25Nb intermetallic by laser powder bed fusion, *Mater. Sci. Eng. A*, 885(2023), art. No. 145652.

[20] E. Liverani, S. Toschi, L. Ceschini, and A. Fortunato, Effect of selective laser melting (SLM) process parameters on micro-structure and mechanical properties of 316L austenitic stainless steel, *J. Mater. Process. Technol.*, 249(2017), p. 255.

[21] L. Hao, W.L. Wang, J. Zeng, M. Song, S. Chang, and C.Y. Zhu, Effect of scanning speed and laser power on formability, microstructure, and quality of 316L stainless steel prepared by selective laser melting, *J. Mater. Res. Technol.*, 25(2023), p. 3189.

[22] M. Sanjari, A. Hadadzadeh, H. Pirgazi, *et al.*, Selective laser melted stainless steel CX: Role of built orientation on microstructure and micro-mechanical properties, *Mater. Sci. Eng. A*, 786(2020), art. No. 139365.

[23] J.W. Liu, Y.N. Song, C.Y. Chen, *et al.*, Effect of scanning speed on the microstructure and mechanical behavior of 316L stainless steel fabricated by selective laser melting, *Mater. Des.*, 186(2020), art. No. 108355.

[24] G.N. Nigon, O. Burkan Isgor, and S. Pasebani, The effect of annealing on the selective laser melting of 2205 duplex stainless steel: Microstructure, grain orientation, and manufacturing challenges, *Opt. Laser Technol.*, 134(2021), art. No. 106643.

[25] P.F. Jiang, C.H. Zhang, S. Zhang, J.B. Zhang, J. Chen, and H.T. Chen, Additive manufacturing of novel ferritic stainless steel by selective laser melting: Role of laser scanning speed on the formability, microstructure and properties, *Opt. Laser Technol.*, 140(2021), art. No. 107055.

[26] T.H. Hsu, P.C. Huang, M.Y. Lee, *et al.*, Effect of processing parameters on the fractions of martensite in 17-4 PH stainless steel fabricated by selective laser melting, *J. Alloys Compd.*, 859(2021), art. No. 157758.

[27] A. Hamada, M. Jaskari, T. Gundgire, and A. Järvenpää, Enhancement and underlying fatigue mechanisms of laser powder bed fusion additive-manufactured 316L stainless steel, *Mater. Sci. Eng. A*, 873(2023), art. No. 145021.

[28] S. Giganto, S. Martínez-Pellitero, J. Barreiro, P. Leo, and M.Á. Castro-Sastre, Impact of the laser scanning strategy on the quality of 17-4PH stainless steel parts manufactured by selective laser melting, *J. Mater. Res. Technol.*, 20(2022), p. 2734.

[29] T.H. Hsu, Y.J. Chang, C.Y. Huang, *et al.*, Microstructure and property of a selective laser melting process induced oxide dispersion strengthened 17-4 PH stainless steel, *J. Alloys Compd.*, 803(2019), p. 30.

[30] W.P. Wu, X. Wang, Q. Wang, *et al.*, Microstructure and mechanical properties of maraging 18Ni-300 steel obtained by powder bed based selective laser melting process, *Rapid Prototyping J.*, 26(2020), No. 8, p. 1379.

[31] J. Song, Q. Tang, Q.X. Feng, *et al.*, Effect of remelting processes on the microstructure and mechanical behaviours of 18Ni-300 maraging steel manufactured by selective laser melting, *Mater. Charact.*, 184(2022), art. No. 111648.

[32] Z.C. Liu, H. Kim, W.W. Liu, W.L. Cong, Q.H. Jiang, and H.C. Zhang, Influence of energy density on macro/micro structures and mechanical properties of as-deposited Inconel 718 parts fabricated by laser engineered net shaping, *J. Manuf. Process.*, 42(2019), p. 96.

[33] T. Rautio, A. Hamada, J. Kumpula, A. Järvenpää, and T. Allam, Enhancement of electrical conductivity and corrosion resistance by silver shell–copper core coating of additively manufactured AlSi10Mg alloy, *Surf. Coat. Technol.*, 403(2020), art. No. 126426.

[34] S.D. Wang, J.H. Wang, S.J. Zhang, *et al.*, Dual nanoprecipitation and nanoscale chemical heterogeneity in a secondary hardening steel for ultrahigh strength and large uniform elongation, *J. Mater. Sci. Technol.*, 185(2024), p. 245.

[35] M. Tanaka and C.S. Choi, The effects of carbon contents and M_s temperatures on the hardness of martensitic Fe–Ni–C alloys, *Trans. Iron Steel Inst. Jpn.*, 12(1972), No. 1, p. 16.

[36] Y.C. Li, W. Yan, J.D. Cotton, *et al.*, A new 1.9GPa maraging stainless steel strengthened by multiple precipitating species, *Mater. Des.*, 82(2015), p. 56.

2486

Int. J. Miner. Metall. Mater., Vol. 31, No. 11, Nov. 2024

[37] W.Q. Guo, B. Feng, Y. Yang, *et al*., Effect of laser scanning speed on the microstructure, phase transformation and mechanical property of NiTi alloys fabricated by LPBF, *Mater. Des.*, 215(2022), art. No. 110460.

[38] R. Esmaeilizadeh, A. Keshavarzkermani, U. Ali, *et al*., Customizing mechanical properties of additively manufactured Hastelloy X parts by adjusting laser scanning speed, *J. Alloys Compd.*, 812(2020), art. No. 152097.

[39] A. Ullah, A. Ur Rehman, M.U. Salamci, F. Pıtır, and T.T. Liu, The influence of laser power and scanning speed on the microstructure and surface morphology of Cu_2O parts in SLM, *Rapid Prototyping J.*, 28(2022), No. 9, p. 1796.

[40] M.M. Chen, R.H. Shi, Z.Z. Liu, *et al*., Phase-field simulation of lack-of-fusion defect and grain growth during laser powder bed fusion of Inconel 718, *Int. J. Miner. Metall. Mater.*, 30(2023), No. 11, p. 2224.

[41] I. Hemmati, V. Ocelík, and J.T.M. De Hosson, Microstructural characterization of AISI 431 martensitic stainless steel laser-deposited coatings, *J. Mater. Sci.*, 46(2011), No. 10, p. 3405.

[42] Y.Y. Chen, H.Y. Yue, and X.P. Wang, Microstructure, texture and tensile property as a function of scanning speed of Ti–47Al–2Cr–2Nb alloy fabricated by selective electron beam melting, *Mater. Sci. Eng. A*, 713(2018), p. 195.

[43] Y.J. Liang, X. Cheng, and H.M. Wang, A new microsegregation model for rapid solidification multicomponent alloys and its application to single-crystal nickel-base superalloys of laser rapid directional solidification, *Acta Mater.*, 118(2016), p. 17.

[44] K.Y. Wang, S.J. Lv, H.H. Wu, *et al*., Recent research progress on the phase-field model of microstructural evolution during metal solidification, *Int. J. Miner. Metall. Mater.*, 30(2023), No. 11, p. 2095.

[45] J.Q. Zhang, M.J. Wang, L.H. Niu, *et al*., Effect of process parameters and heat treatment on the properties of stainless steel CX fabricated by selective laser melting, *J. Alloys Compd.*, 877(2021), art. No. 160062.

[46] S. Afkhami, V. Javaheri, E. Dabiri, H. Piili, and T. Björk, Effects of manufacturing parameters, heat treatment, and machining on the physical and mechanical properties of 13Cr10Ni1.7Mo2Al0.4Mn0.4Si steel processed by laser powder bed fusion, *Mater. Sci. Eng. A*, 832(2022), art. No. 142402.

[47] D.C. Kong, C.F. Dong, X.Q. Ni, *et al*., Mechanical properties and corrosion behavior of selective laser melted 316L stainless steel after different heat treatment processes, *J. Mater. Sci. Technol.*, 35(2019), No. 7, p. 1499.

[48] C. Chang, X.C. Yan, R. Bolot, *et al*., Influence of post-heat treatments on the mechanical properties of CX stainless steel fabricated by selective laser melting, *J. Mater. Sci.*, 55(2020), No. 19, p. 8303.

[49] J. Su, M. Sanjari, A.S.H. Kabir, *et al*., Characteristics of magnesium AZ31 alloys subjected to high speed rolling, *Mater. Sci. Eng. A*, 636(2015), p. 582.

[50] W. Zhao, H.L. Xiang, R.X. Yu, and G. Mou, Effects of laser scanning speed on the microstructure and mechanical properties of 2205 duplex stainless steel fabricated by selective laser melting, *J. Manuf. Process.*, 94(2023), p. 1.

[51] Y.M. Wang, T. Voisin, J.T. McKeown, *et al*., Additively manufactured hierarchical stainless steels with high strength and ductility, *Nat. Mater.*, 17(2018), p. 63.

[52] D.C. Kong, C.F. Dong, S.L. Wei, *et al*., About metastable cellular structure in additively manufactured austenitic stainless steels, *Addit. Manuf.*, 38(2021), art. No. 101804.

[53] K.G. Prashanth, S. Scudino, T. Maity, J. Das, and J. Eckert, Is the energy density a reliable parameter for materials synthesis by selective laser melting? *Mater. Res. Lett.*, 5(2017), No. 6, p. 386.

[54] M. Yakout, M.A. Elbestawi, and S.C. Veldhuis, A study of thermal expansion coefficients and microstructure during select-ive laser melting of Invar 36 and stainless steel 316L, *Addit. Manuf.*, 24(2018), p. 405.

[55] J.L. Bartlett, F.M. Heim, Y.V. Murty, and X.D. Li, *In situ* defect detection in selective laser melting via full-field infrared thermography, *Addit. Manuf.*, 24(2018), p. 595.

[56] R. Cunningham, C. Zhao, N. Parab, *et al*., Keyhole threshold and morphology in laser melting revealed by ultrahigh-speed X-ray imaging, *Science*, 363(2019), No. 6429, p. 849.

[57] D.M. Li, X. Zhang, R.X. Qin, J.X. Xu, D.Y. Yue, and B.Z. Chen, Influence of processing parameters on AlSi10Mg lattice structure during selective laser melting: Manufacturing defects, thermal behavior and compression properties, *Opt. Laser Technol.*, 161(2023), art. No. 109182.

[58] F.Z. Chu, E.L. Li, H.P. Shen, *et al*., Influence of powder size on defect generation in laser powder bed fusion of AlSi10Mg alloy, *J. Manuf. Process.*, 94(2023), p. 183.

[59] J. Chao, D.G. Morris, M.A. Muñoz-Morris, and J.L. Gonzalez-Carrasco, The influence of some microstructural and test parameters on the tensile behaviour and the ductility of a mechanically-alloyed Fe–40Al alloy, *Intermetallics*, 9(2001), No. 4, p. 299.

[60] Q.D. Yang, S. Yang, S.Y. Ma, *et al*., *In-situ* X-ray computed tomography tensile tests and analysis of damage mechanism and mechanical properties in laser powder bed fused Invar 36 alloy, *J. Mater. Sci. Technol.*, 175(2024), p. 29.

[61] J. Kwon, Y.T. Choi, E.S. Kim, *et al*., Effect of cell characteristics on mechanical properties of AlSi10Mg alloy fabricated by laser powder bed fusion, *Mater. Sci. Eng. A*, 901(2024), art. No. 146537.

[62] W.S. Tang, X.Q. Yang, C.B. Tian, and C. Gu, Effect of rotation speed on microstructure and mechanical anisotropy of Al-5083 alloy builds fabricated by friction extrusion additive manufacturing, *Mater. Sci. Eng. A*, 860(2022), art. No. 144237.

[63] S. Morito, H. Yoshida, T. Maki, and X. Huang, Effect of block size on the strength of lath martensite in low carbon steels, *Mater. Sci. Eng. A*, 438-440(2006), p. 237.

[64] T.Q. Liu, Z.X. Cao, H. Wang, G.L. Wu, J.J. Jin, and W.Q. Cao, A new 2.4 GPa extra-high strength steel with good ductility and high toughness designed by synergistic strengthening of nanoparticles and high-density dislocations, *Scripta Mater.*, 178(2020), p. 285.

[65] J. Haubrich, J. Gussone, P. Barriobero-Vila, *et al*., The role of lattice defects, element partitioning and intrinsic heat effects on the microstructure in selective laser melted Ti–6Al–4V, *Acta Mater.*, 167(2019), p. 136.

[66] M.C. Niu, G. Zhou, W. Wang, M.B. Shahzad, Y.Y. Shan, and K. Yang, Precipitate evolution and strengthening behavior during aging process in a 2.5 GPa grade maraging steel, *Acta Mater.*, 179(2019), p. 296.

[67] E.I. Galindo-Nava and P.E.J. Rivera-Díaz-del-Castillo, A model for the microstructure behaviour and strength evolution in lath martensite, *Acta Mater.*, 98(2015), p. 81.

[68] V.K. Vasudevan, S.J. Kim, and C.M. Wayman, Precipitation reactions and strengthening behavior in 18 Wt Pct nickel maraging steels, *Metall. Trans. A*, 21(1990), No. 10, p. 2655.

[69] R.L. Fleischer, Substitutional solution hardening, *Acta Metall.*, 11(1963), No. 3, p. 203.

[70] R. Labusch, A statistical theory of solid solution hardening, *Phys. Status Solidi B.*, 41(1970), No. 2, p. 659.

[71] E.I. Galindo-Nava and P.E.J. Rivera-Díaz-del-Castillo, Understanding the factors controlling the hardness in martensitic steels, *Scripta Mater.*, 110(2016), p. 96.

[72] G. Ghosh and G.B. Olson, Kinetics of F.C.C. → B.C.C. heterogeneous martensitic nucleation—I. The critical driving force for athermal nucleation, *Acta Metall. Mater.*, 42(1994), No. 10, p. 3361.

[73] P. Peng, K.S. Wang, W. Wang, *et al*., Relationship between mi-

crostructure and mechanical properties of friction stir processed AISI 316L steel produced by selective laser melting, *Mater. Charact.*, 163(2020), art. No. 110283.

[74] H.H. Jin, E. Ko, J. Kwon, S.S. Hwang, and C. Shin, Evaluation of critical resolved shear strength and deformation mode in proton-irradiated austenitic stainless steel using micro-compression tests, *J. Nucl. Mater.*, 470(2016), p. 155.

[75] B.Q. Han and D.C. Dunand, Creep of magnesium strengthened with high volume fractions of yttria dispersoids, *Mater. Sci.* *Eng. A*, 300(2001), No. 1-2, p. 235.

[76] Y. Xiang, Modeling dislocations at different scales, *Commun. Comput. Phys.*, 1(2006), No. 3, p. 383.

[77] B. Kim, E. Boucard, T. Sourmail, D. San Martín, N. Gey, and P.E.J. Rivera-Díaz-del-Castillo, The influence of silicon in tempered martensite: Understanding the microstructure–properties relationship in 0.5–0.6wt.% C steels, *Acta Mater.*, 68(2014), p. 169.